AGU ADVANCING EARTH AND SPACE SCIENCE

Geophysical Research Letters

RESEARCH LETTER
10.1029/2020GL088656

Raindrop Signature from Microwave Radiometer Over Deserts

Yalei You[1], S. Joseph Munchak[2], Ralph Ferraro[3], Karen Mohr[2], Christa Peters-Lidard[2], Catherine Prigent[4], Sarah Ringerud[2,5], Scott Rudlosky[3], Heshun Wang[1], Hamidreza Norouzi[6], and Satya Prakash[7]

[1]Earth System Science Interdisciplinary Center/Cooperative Institute for Climate and Satellites, University of Maryland, College Park, MD, USA, [2]NASA Goddard Space Flight Center, Greenbelt, MD, USA, [3]NOAA/NESDIS/STAR, College Park, MD, USA, [4]Sorbonne Universite, Observatoire de Paris, Universite PSL, CNRS, LERMA, Paris, France, [5]Earth System Science Interdisciplinary Center, University of Maryland, College Park, MD, USA, [6]New York City College of Technology, New York, NY, USA, [7]Divecha Centre for Climate Change, Indian Institute of Science, Bengaluru, India

Key Points:
- Time series analyses reveal a TB increase at H19 due to raindrop emission as the primary cloud signature over deserts
- Low surface emissivity supports the use of raindrop emission as the primary signature over deserts
- Surface rain rate better correlates with the raindrop emission signal than with the scattering induced by ice further aloft

Correspondence to:
Y. You,
yyou@umd.edu

Citation:
You, Y., Munchak, S. J., Ferraro, R., Mohr, K., Peters-Lidard, C., Prigent, C., et al. (2020). Raindrop signature from microwave radiometer over deserts. *Geophysical Research Letters*, *47*, e2020GL088656. https://doi.org/10.1029/2020GL088656

Received 30 APR 2020
Accepted 23 JUL 2020
Accepted article online 29 JUL 2020

Abstract Rainfall estimates from spaceborne microwave radiometers form the foundation of global precipitation data sets. Since the beginning of the satellite microwave rainfall estimation era in the 1980s, the primary signature leveraged over land for these estimates has been the brightness temperature (TB) depression due to ice particle scattering. Contrary to this practice, time series analyses based on observations from two spaceborne radars and two spaceborne radiometers reveal a TB increase at H19 due to raindrop emission as the primary cloud particle signature over desert terrain. Low surface emissivity supports the use of liquid raindrop emission as the primary signature over desert surfaces. In these regions, the surface rain rate better correlates with the liquid raindrop emission signal than with the scattering induced by ice further aloft, suggesting a new potential for improving rainfall estimation over deserts by exploiting the liquid raindrop emission signature.

Plain Language Summary Global rainfall mapping is a very challenging task since ground-based observations from radars or rain-gauges are limited or unavailable over many regions (e.g., desert). Satellite observations provide the unique opportunity to map the rainfall over these regions. Deserts cover about one third of the Earth's land surface, while the current satellite rainfall estimate techniques over deserts relate the ice particles aloft with surface rain rates, leading to large estimation uncertainties. This study for the first time reports the liquid raindrop signature over deserts from the satellite observations, which could represent a fundamental algorithm change over deserts when estimating rainfall from space.

1. Introduction

Passive microwave radiometers are utilized by meteorological agencies worldwide to remotely sense precipitation from space (Goldberg, 2018; Levizzani et al., 2018; Skofronick-Jackson et al., 2017). More than 30 radiometers onboard satellites from several international agencies have been used for rainfall measurement since the 1980s, with about 15 currently operational and several follow-on missions being planned (Goldberg, 2018; Gu & Tong, 2015; Hou et al., 2014; Skofronick-Jackson et al., 2017). Rainfall estimates from these radiometer observations make it possible to generate the widely used hourly (or half-hour) global precipitation data sets (Huffman et al., 2007, 2015; Joyce et al., 2004; Kubota et al., 2007; Xie et al., 2017).

Many retrieval algorithms have been developed to estimate rain rates from the radiometer-observed brightness temperature (TB) fields since the beginning of the satellite microwave rainfall estimation era (e.g., Aonashi & Liu, 2000; Ebtehaj et al., 2015; Ferraro et al., 1994; Kummerow et al., 1996, 2011; Laviola & Levizzani, 2011; Sano et al., 2013; Spencer et al., 1989; You et al., 2015). The TB fields observed by the radiometer are a result of the radiation scattering/emission effects of all the hydrometeors within the atmospheric column in the radiometer field of view (You & Liu, 2012).

Over ocean, retrieval algorithms relate the liquid raindrop emission signatures primarily at the low-frequency channels (<85 GHz) to surface rain rates with little interference from surface emission due to the low and relatively uniform oceanic surface emissivity (Aonashi et al., 2009; Kummerow et al., 2015; Liu & Curry, 1992). In contrast, land surface emissivity is generally rather high and highly

inhomogeneous (Ferraro et al., 2013; Munchak et al., 2020; Prakash et al., 2018; Prigent et al., 2006; Turk et al., 2014). It has long been observed that the primary signature over land is the TB depression at the high-frequency channels (≥89 GHz) due to the ice particle scattering (Grody, 1991; Petty, 1995; Wilheit, 1986; You et al., 2015, 2016). Several previous studies also exploited the ice scattering signature at 37 GHz (Dinku & Anagnostou, 2005; Spencer et al., 1983). Hence, current over-land retrieval algorithms relate the scattering of radiation by ice particles aloft with the surface rain rate. Because liquid raindrops have a better correlation with the surface rain rate than the ice particles aloft, previous validation studies have confirmed that the estimated rain rates over ocean from passive microwave radiometers are more accurate than those over land (Aonashi et al., 2009; Kummerow et al., 2015; You, Petkovic, et al., 2020; You, Wang, et al., 2020).

Due to the high and highly inhomogeneous land surface emissivity, the common practice is to utilize the TB depression primarily at high-frequency channels (≥85 GHz) caused by the ice particle scattering. By using observations from two spaceborne radars and two spaceborne radiometers, we show that the TB increase signature at low-frequency horizontal polarized channels is apparent in the TB time series over large areas of some world deserts, owning to the low microwave emissivity at the horizontal polarization for satellite incidence angles close to 50° (Grody & Weng, 2008; Munchak et al., 2020; Prigent et al., 2006; Turk et al., 2014).

Deserts cover about one third of the Earth's land surface, where rainfall estimates from spaceborne radiometers have large uncertainties (Dinku et al., 2010; Maggioni et al., 2016; You, Wang, et al., 2020). This study suggests a new potential for improving rainfall estimation over deserts by exploiting the liquid raindrop emission signature. We also demonstrate that this TB increase signal correlates more strongly with the liquid water path and the surface rain rate, compared with the ice water path.

2. Data and Methods

2.1. Two Spaceborne Radars and Two Spaceborne Radiometers

We use the TB observations of Advanced Microwave Scanning Radiometer for the Earth Observing System (AMSR-E) onboard the Aqua satellite (Kawanishi et al., 2003) and the radar reflectivity of the Cloud Profiling Radar (CPR) onboard the CloudSat satellite (Stephens et al., 2002) from April 2006 to April 2011 when both instruments functioned normally. Both Aqua and CloudSat are A-Train satellite constellation members with CloudSat lagging Aqua by at most 2 min (Stephens et al., 2002). Due to the short time difference (<2 min, within the convective time scale), this study considers the observations from AMSR-E and CPR as simultaneous. Both satellites are in sun-synchronous orbits, meaning that they pass over a given location at a fixed time, typically in the morning and then in the evening. We choose the sun-synchronous satellites to minimize the land surface temperature (LST) influence on the TB observations.

CloudSat makes measurements at nadir (~1.6 km) within the wide AMSR-E swath (~1,450 km), so AMSR-E TBs can be assigned to any CloudSat profile. For AMSR-E, we use the calibrated TB (Berg et al., 2016) at 10.7 (V/H), 18.7 (V/H), 23.8 (V/H), 36.5 (V/H), and 89.0 (V/H) GHz channels (V/H, vertical/horizontal polarization). Hereafter, these channels are referred to as V10/H10, V19/H19, V24/H24, V37/H37, and V89/H89. For CPR, we use the radar reflectivity (dBZ) at the near-surface level from 2B-GEOPROF (Marchand et al., 2008), which is about 1.5 km above the ground level.

To more clearly demonstrate the liquid water information, we also use the TB from the Global Precipitation Measurement (GPM) Imager (GMI) (Draper et al., 2015) and the rainfall-related variables (liquid water path, surface rain rate, and ice water path) from Ku-band precipitation radar (KuPR) (Hou et al., 2014) from March 2014 to December 2019. Both GMI and KuPR are onboard the GPM Core Observatory satellite with a non-sun-synchronous orbit which can fly over a location at any time of the day. For GMI, we use TB at 10.7 (V/H), 18.7 (V/H), 36.5 (V/H), 89.0 GHz (V/H), and 183.3±7 (V). These channels are referred to as V10/H10, V19/H19, V37/H37, V89/H89, and V190. We select the high-frequency channel of 89 and 190 GHz, since channel at 89 GHz is commonly available for many passive microwave radiometers from the beginning of the satellite rainfall observation era, and V190 channel is the highest frequency available on GMI. Both channels are primarily sensitive to the ice scattering. For KuPR, we use the liquid water path (i.e., integrated liquid water content), the ice water path (i.e., integrated ice water content), and the surface rain rate.

The hourly LST at $0.5° \times 0.625°$ is from the Modern-Era Retrospective Analysis for Research and Applications-2 (MERRA-2) (Gelaro et al., 2017).

2.2. Collocation Methods

To mitigate the possible influence of the different footprint sizes, we convolve the AMSR-E higher resolution observations (37 and 89 GHz) to the resolution of the 19 GHz footprint size (~21 km) as the nominal resolution. Specifically, the native resolutions are ~11 and ~5 km for 37 and 89 GHz. We average the nearest four $[(21/11)^2 \approx 4]$ 37 GHz pixels and the nearest 18 $[(21/5)^2 \approx 18]$ 89 GHz pixels to roughly match the area of 19 GHz footprint size (i.e., $21 \times 21 = 441\ km^2$). The spatial resolution at 10 and 24 GHz are about 42 and 26 km, which are kept unchanged. For CPR, we average 11 pixels inside each AMSR-E field of view (FOV).

Similar downgrading strategies are applied to the GMI frequencies and KuPR observations. The footprint sizes are 25, 15, 12, 7, and 6 km for 10, 19, 37, 89, and 190 GHz, respectively. We take 19 GHz (15 km) as the nominal resolution. The footprint sizes from 10 and 37 GHz remain unchanged, while we average the nearest 5 $[(15/7)^2 \approx 5]$ 89 GHz pixels and 7 $[(15/6)^2 \approx 7]$ 190 GHz pixels to roughly match the area of 19 GHz footprint size. For KuPR-related variables with a 5.2 km footprint size, we average the nearest 9 $[(15/5.2)^2 \approx 9]$ KuPR pixels to roughly match the area of the 19 GHz footprint size. Since GMI has a much larger swath width (904 km) than KuPR (245 km), only the GMI observations with KuPR coverage are selected in this study.

For MERRA-2 LST, we use the nearest grid cell to match the satellite observations at the closest time.

3. Results

3.1. TB Increase at H19 Due To the Raindrop Emission

This section begins with a time series case study analysis of 19 GHz TB observations, which shows that over desert terrain, H19 indicates an unexpected warming signature between subsequent overpasses. Our analyses reveal this signal to be associated with liquid water emissions from cloud and precipitation particles rather than increases in the surface emissivity or LST. This finding provides a new opportunity to improve our understanding of the frequency and magnitude of precipitation over large desert regions.

Figure 1a shows the time series from AMSR-E TB observations at the vertically and horizontally polarized 19 GHz (V19 and H19) channels and the MERRA-2 LST time series in 2009 for a 0.25° degree grid box (21.5–21.75°N, 14.5–14.75°E) in the Sahara Desert around local midnight (00:40). We choose this grid box since there is a coincident raining event observed by the spaceborne CPR at this location. The geospatial distribution of all the similar cases is shown in Figure 2.

The most prominent features are H19 TB increases of about 10, 18, 8, and 14 K on 10 April 2009, 7 May 2009, 24 June 2009, and 1 September 2009, respectively, relative to the same overpass on the preceding day at the same time (indicated by black crosses on Figure 1a). There are three possible reasons why H19 TB can increase by this magnitude: the surface emissivity increase, LST increase, and the liquid water emission. First, we can rule out the surface emissivity increase since the surface in this remote Sahara Desert location is sand and bare rock throughout the year. The normalized difference vegetation index (NDVI) indicates no vegetation growth in this location throughout 2009. Second, LST on these four occasions varies less than 3 K compared with their preceding days at 00:40, shown in the LST time series (Figure 1a). Radiation at 19 GHz can penetrate the land surface to several centimeters below the surface and is more sensitive to the soil temperature within that layer. The MERRA-2 soil temperature shows an even smaller temporal variation below the surface, consistent with previous studies (Grody & Weng, 2008; Norouzi et al., 2012). We hypothesize that emission from liquid raindrops is the best explanation for an increase in H19 of the magnitude shown in Figure 1a. CPR observed surface rainfall with radar reflectivity of −4.1 dBZ on 1 September (indicated by a purple circle on Figure 1a). There are no coincident CPR observations for the other three events.

We also notice a clearly evident TB depression at V19 on 1 September, though the TB depression magnitude (5 K) compared with the preceding overpass is smaller than the H19 increase (14 K). The fundamental reason why the liquid raindrop emission leads to an opposite response at H19 (increase) and V19 (decrease) lies in the large emissivity difference between H19 and V19. In other words, the small surface emissivity at H19 (close to 0.8) provides a colder land surface emission background so that the "raindrop" emission (which can be approximated as the mean temperature from the melting level to the surface) appears "warmer," leading to a TB increase at H19. In contrast, the large surface emissivity at V19 (close to 1.0) provides a warmer land surface emission background so the "raindrop" emission appears "colder," leading to a TB depression at V19.

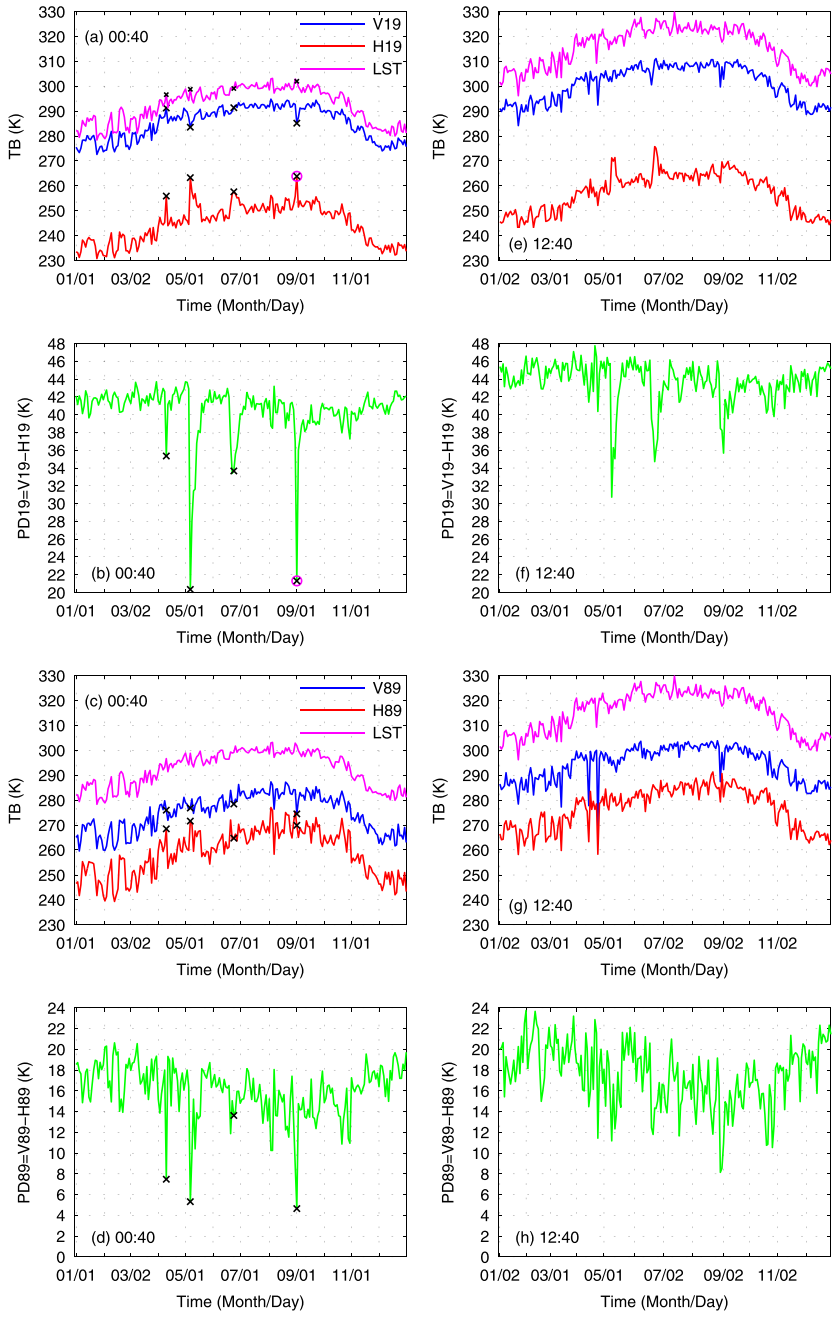

Figure 1. (a–d) Time series at the location of (21.5–21.75°N,14.5–14.75°E) in the Sahara desert around midnight (00:40) for V19, H19, LST, V89, H89, and PD89. The black crosses indicate the four occasions on 10 April 2009, 7 May 2009, 24 June 2009, and 1 September 2009. The purple circle on panels (a) and (b) indicates that CPR observed surface rainfall with radar reflectivity of −4.1 dBZ on 1 September 2009. (e–h) Same as the first column except around noon (12:40).

Rainfall can increase the surface soil moisture quickly and dramatically (Yin et al., 2019), leading to an emissivity drop at both V19 and H19 (Jackson, 1993; Li & Min, 2013; Munchak et al., 2020; You et al., 2014). However, this emissivity drop is entirely consistent with our hypothesis that emission from liquid raindrops is responsible for the TB increase at H19. The smaller surface emissivity itself due to the rainfall impact would result in a TB decrease at H19. Therefore, the observed TB increase at H19 is most likely caused by the liquid raindrop emission. In this case, the smaller land surface emissivity makes the liquid raindrop

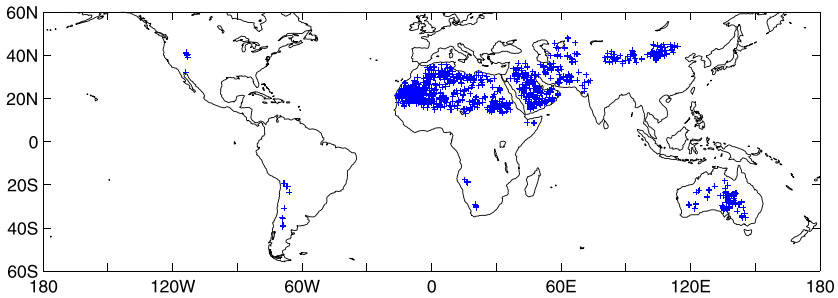

Figure 2. The location where PD19 monthly anomaly drops at least 10 K when CPR indicates the surface rain rate.

emission signature even more evident at H19 (similar to over ocean). Whether we can observe the liquid raindrop emission signal (causing TB increase) depends on how low the emissivity can become under the raining condition. For V19, it is unlikely that the emissivity becomes low enough (from close to 1 to close to 0.9) for the aforementioned cases so that the liquid raindrop emission signal is observable. However, the lower emissivity due to the rainfall impact may also contribute to the TB drop at V19.

The polarization difference (PD) between V19 and H19 (PD19 = V19 − H19) is used to minimize the LST seasonal variation and to better capture the TB increase signature. The PD19 time series clearly indicate that PD19 remains at 42 K with an abrupt drop on the previously mentioned four days at 00:40 (Figure 1b). The PD19 drops from 42 to 35, 20, 34, and 21 K. As discussed earlier, the most likely explanation for these sharp drops is the liquid raindrop emission (essentially unpolarized) causing the H19 to increase, which reduces the strong PD between horizontal and vertical polarized channels from the land surface. This feature (raindrop emission leading to the PD drop) is commonly observed over ocean. In this sense, the strongly polarized desert surface is similar to the ocean surface. CPR observations also confirm the presence of the liquid raindrops on 1 September (purple circle in Figure 1b).

In this desert location, the relatively low surface emissivity at H19 allows identification of the TB increases related to liquid raindrop emissions (sudden PD19 drops). Radiative transfer model simulations have provided insight into this phenomenon. Spencer et al. (1989) has shown that over the oceans, where surface emissivity is low (~0.50), the H19 can increase as much as 50 K due to the raindrop emission. You et al. (2018) showed that the H19 increase is evident when the land emissivity is less than 0.9 and the rainfall intensity is less than 4 mm/hr over the Southern Great Plains. Similarly, Munchak et al. (2020) demonstrated that the liquid water clouds can increase TB when emissivity is less than 0.9 and can decrease TB when emissivity is greater than 0.95. Although most land surfaces have microwave emissivities in or near this range (greater than 0.90 while less than 0.95), rendering liquid clouds and rain undetectable by microwave TB, deserts have H19 emissivities of about 0.80 (Norouzi et al., 2012; Prigent et al., 2006). Although these model simulations predict a liquid raindrop emission signature under the low surface emissivity background, this study for the first time (to the best of our knowledge) reports the liquid raindrop signal over such large areas (desert) over land from satellite observations.

In cases where precipitation systems have weak ice scattering signatures and light rainfall, the signal from raindrop emission at H19 may be more apparent than the signal from ice scattering at 89 GHz. Figure 1c confirms that the ice scattering signature at the high-frequency channel (89 GHz) is weak. From the time series of both V89 and H89, there is no evident TB depression signal on the previously mentioned four occasions. Specifically, TB at V89 drops about 4, 2, 2, and 8 K, respectively, on the previously mentioned four occasions (marked as the black crosses in Figure 1c) compared with their preceding day overpasses, while TB at H89 varies about 6, 10, 1, and −6 K. Since ice particle scattering cross sections are much smaller at 19 GHz than 89 GHz (Liu, 2008), we conclude there is little impact of ice scattering on the TB or PD on these days at 19 GHz. The PD at 89 GHz (PD89) shows a noticeable drop on 7 May and 1 September, but its magnitude is much smaller than that from PD19 (cf. Figures 1b and 1d).

Similarly, the TB observations at the same location in the afternoon (12 hr later at 12:40) also show clear H19 increase (Figure 1e) and PD19 decrease (Figure 1f) on 10 May and 25 June but of different magnitudes—indeed, the 10 April event (occurred in the morning around 00:40) is barely discernible. This also suggests

that the PD19 drop is due to the microwave emission of the falling raindrops, which is a short-lived event and not an effect of rain on the surface, which would have a more persistent impact. As expected, the liquid raindrop emission signature on these two occasions is not captured by V89, H89, or PD89 (Figures 1g and 1h), which primarily respond to the ice particle scattering signature.

Time series analyses at 10, 24, and 37 GHz also reveal evident PD drop on the aforementioned four days, though the magnitude of the drop is not as large as that from 19 GHz. For 10 GHz, its longer wavelength makes it not as sensitive as 19 GHz to the liquid raindrop emission, though the PD from 10 GHz itself (PD10 = V10 − H10) is larger than PD19. Compared with 19 GHz, the relatively smaller PD drop from 24 and 37 GHz on the aforementioned four days is because both frequencies are less strongly polarized than 19 GHz, reducing the potential to increase horizontal polarized TB and decrease PD via microwave emission by the falling rain.

The following analysis uses PD19, instead of H19 or V19, to mitigate the LST influence. For example, both V19 and H19 at 00:40 are consistently 20 K colder than those at 12:40 (c.f., Figures 1a and 1e) due to the LST diurnal cycle. The large TB difference at different times of day is mitigated by using PD19, which is about 42 and 45 K at 00:40 and 12:40 under no-rain conditions (cf. Figures 1b and 1f).

3.2. Where the Liquid Raindrop Signal Exists

To find where this liquid raindrop signal exists, we check the PD19 monthly anomaly based on AMSR-E observations for all raining observations indicated by the CPR reflectivity greater than −15 dBZ over the CPR observation domain (82°S to 82°N, except over the snow-covered regions). For each raining observation, we compute the difference between PD19 and the monthly mean PD19 at that location.

The locations of all PD19 decreases of at least 10 K show strong coincidence with large desert regions (Figure 2). In these desert regions, liquid raindrop emissions increase H19 and decrease V19 (leading to a sharp PD19 drop), as shown in the case study (Figure 1). The fundamental reason why the liquid raindrop information can be captured by the microwave radiometer over deserts is because the surface emissivity at H19 over many types of desert surfaces is low (∼0.8) (Grody & Weng, 2008; Munchak et al., 2020; Prigent et al., 2006) and remains relatively constant. Therefore, the radiometrically warm raindrop signal is evident compared to those desert surface types that are radiometrically cold at H19. In contrast, the surface emissivity over other types of land surface, particularly surfaces with vegetation, are radiometrically warm in the same channels, with emissivities close to 1, therefore masking out the warm raindrop signal.

3.3. PD19 Anomaly Correlates With Rainfall-Related Variables

To offer additional evidence that PD19 captures the liquid raindrop emission signature, we calculate the correlation between PD19 (derived from GMI observations) and precipitation properties (derived from KuPR). The correlation is calculated only when the raining sample size is greater than 30 in a certain 0.25° grid box.

Figure 3a shows the correlation between the PD19 monthly anomaly with liquid water path at each 0.25 grid box over the desert regions. Evidently, the PD19 anomaly has a stronger correlation with the liquid water path, compared with either V89 (Figure 3b) or V190 (Figure 3c). V89 is a channel common to most passive microwave radiometers, and V190 is the highest available channel from GMI. Both channels primarily capture the ice scattering signature.

Since the PD19 anomaly captures the liquid water information, we expect that it has a better correlation with the surface rain rate. Indeed, Figure 3d shows that the PD19 anomaly correlates more strongly with the surface rain rate, compared with either V89 (Figure 3e) or V190 (Figure 3f). V89 and V190 are primarily sensitive to the ice particles aloft, which is confirmed by the much larger correlation between V89 and ice water path and between V190 and the ice water path, compared with that from the PD19 anomaly (cf. Figures 3h and 3g and Figures 3i and 3g).

4. Discussion

It has long been believed that the TB depression due to the ice scattering at the high-frequency channels (≥85 GHz) is the primary signature over land for rainfall estimation. This study presents observations showing the contrary over some desert regions: The raindrop emission, leading to the H19 increase and the PD19 sharp drop, is the primary signature. This raindrop emission signature can be well captured by analyzing the

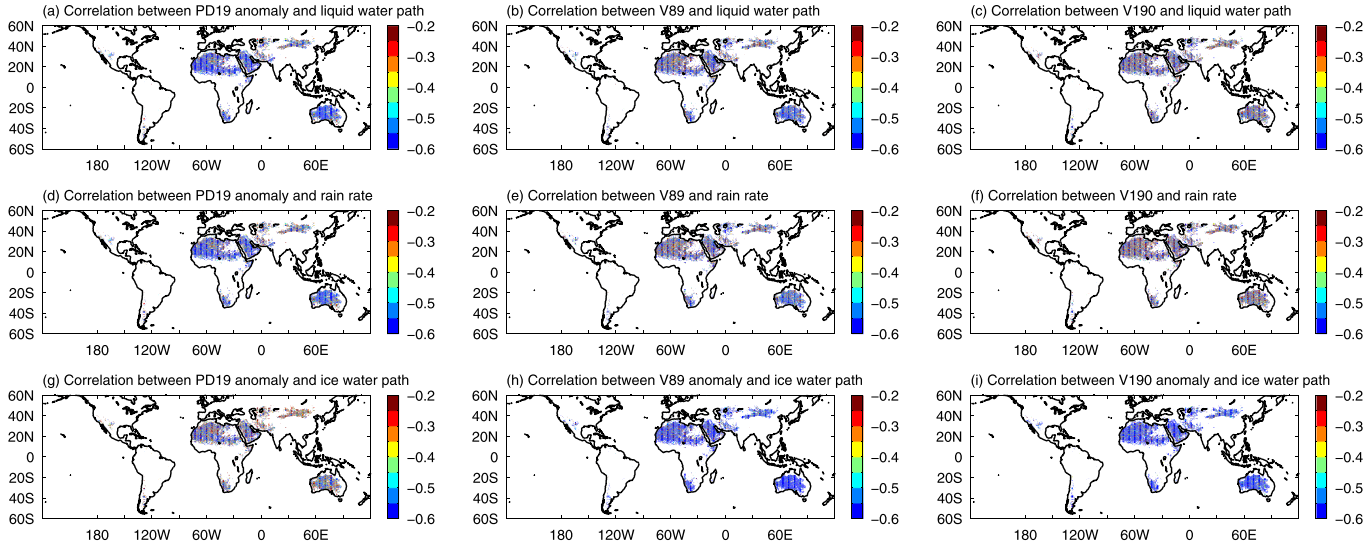

Figure 3. (a, d, g) Correlation between PD19 anomaly and the liquid water path, between PD19 anomaly and the surface rain rate, and between PD19 anomaly and the ice water path. (b, e, h) Same as panels (a), (d), and (g) except for V89. (c, f, i) Same as panels (a), (d), and (g) except for V190.

PD19 time series. The better correlation between PD19 monthly anomaly and the liquid water path (or the surface rain rate) further confirms that rain can be directly detected via the PD19, rather than inferred from higher-frequency (e.g., V89 and V190) scattering, which is a proxy for the ice water path. Our study has shown potential to improve rainfall estimation over desert by identifying surfaces where exploiting the rain drop emission signature is possible. Over these arid regions, previous validation studies consistently showed poor rainfall retrieval performance from the microwave radiometer due to the weak scattering signature (Dinku et al., 2010; Maggioni et al., 2016; You, Wang, et al., 2020). This study also highlights the importance of analyzing TB time series in precipitation estimation work (You et al., 2017, 2018).

This study demonstrates a new idea to observe rainfall over some deserts where microwave emissivity is low enough (~0.8) so that the liquid raindrop signature can be captured by the PD temporal variation. While rainfall is less frequent and often lighter in deserts compared to other regions, Kelley (2014) documented an apparent rainfall seasonal variation even over the driest part of the Sahara Desert. Further, rainfall shapes the biodiversity distribution over deserts by maintaining the delicate balance between the plant growth/availability and the abundance of herbivores (Marshal et al., 2002; Vale & Brito, 2015). Previous studies demonstrated that desert-adapted species are disproportionately vulnerable to changes in precipitation in a warming climate (Nafus et al., 2017; Vale & Brito, 2015). This study has the potential to improve rainfall estimates from satellite observations and thus enable us to better monitor and assess the impacts of changes in rainfall on desert biodiversity.

Finally, it should be noted that the spaceborne radar provides the near-surface observations (about 1.5 km above the ground), due to the clutter contamination at the range gates closer to the ground. These observations are often taken as the "reference" in the precipitation estimation community. Considering the intense under-cloud evaporation in the dry desert climate, some of these raindrops may not reach the ground, leading to the so-called "virga" precipitation (Wang et al., 2018). Nevertheless, liquid raindrops in the air are more closely related to the surface rain rate, compared to the ice particles further away from the surface. Future plans include (1) to compare this emission signature from PD19 and the scattering signature from high frequency channels (e.g., V190) relative to the in-situ gauge/radar observations over desert regions at the monthly scale and (2) to search this emission signature over other land surfaces with emissivity at H19 close to 0.8 due to the previous rainfall events.

Data Availability Statement

GPM and AMSR-E data are downloaded from NASA Precipitation Processing System (PPS) website (https://storm.pps.eosdis.nasa.gov/storm/). CloudSat data are downloaded from Cloudsat Data Processing Center

(http://www.cloudsat.cira.colostate.edu/order-data). MERRA-2 data are downloaded from NASA Goddard Earth Sciences (GES) Data and Information Services Center (DISC) (https://gmao.gsfc.nasa.gov/reanalysis/MERRA-2/).

Acknowledgments
This work is supported by NASA's Precipitation Measurement Missions Program science team under the management of Dr. Gail Skofronick-Jackson via the Internal Scientist Funding Model. Y. Y. also would like to acknowledge the financial support from NOAA Grant NA19NES4320002 (Cooperative Institute for Satellite Earth System Studies-CISESS) at the University of Maryland/ESSIC.

References

Aonashi, K., Awaka, J., Hirose, M., Kozu, T., Kubota, T., Liu, G., et al. (2009). GSMaP passive microwave precipitation retrieval algorithm: Algorithm description and validation. *Journal of the Meteorological Society of Japan*, *87*(0), 119–136.

Aonashi, K., & Liu, G. (2000). Passive microwave precipitation retrievals using TMI during the Baiu period of 1998. Part I: Algorithm description and validation. *Journal of Applied Meteorology*, *39*(12), 2024–2037.

Berg, W., Bilanow, S., Chen, R., Datta, S., Draper, D., Ebrahimi, H., et al. (2016). Intercalibration of the GPM microwave radiometer constellation. *Journal of Atmospheric and Oceanic Technology*, *33*(12), 2639–2654.

Dinku, T., & Anagnostou, E. N. (2005). Regional differences in overland rainfall estimation from PR-calibrated TMI algorithm. *Journal of Applied Meteorology*, *44*(2), 189–205.

Dinku, T., Ceccato, P., Cressman, K., & Connor, S. J. (2010). Evaluating detection skills of satellite rainfall estimates over desert locust recession regions. *Journal of Applied Meteorology and Climatology*, *49*(6), 1322–1332.

Draper, D. W., Newell, D., Wentz, F. J., Krimchansky, S., & Skofronick-Jackson, G. M. (2015). The Global Precipitation Measurement (GPM) Microwave Imager (GMI): Instrument overview and early on-orbit performance. *IEEE Journal of Selected Topics in Applied Earth Observations in Remote Sensing*, *8*, 3452–3462.

Ebtehaj, A. M., Bras, R. L., & Foufoula-Georgiou, E. (2015). Shrunken locally linear embedding for passive microwave retrieval of precipitation. *IEEE Transactions on Geoscience and Remote Sensing*, *53*(7), 3720–3736.

Ferraro, R. R., Grody, N. C., & Marks, G. F. (1994). Effects of surface conditions on rain identification using the DMSP-SSM/I. *Remote Sensing Reviews*, *11*(1-4), 195–209.

Ferraro, R. R., Peters-Lidard, C. D., Hernandez, C., Turk, F. J., Aires, F., Prigent, C., et al. (2013). An evaluation of microwave land surface emissivities over the continental United States to benefit GPM-era precipitation algorithms. *IEEE Transactions on Geoscience and Remote Sensing*, *51*(1), 378–398.

Gelaro, R., McCarty, W., Suárez, M. J., Todling, R., Molod, A., Takacs, L., et al. (2017). The modern-era retrospective analysis for research and applications, version 2 (MERRA-2). *Journal of Climate*, *30*(14), 5419–5454.

Goldberg, M. (2018). The Joint Polar Satellite System Overview. In *IGARSS 2018-2018 IEEE International Geoscience and Remote Sensing Symposium* (pp. 1581–1584). EEE.

Grody, N. C. (1991). Classification of snow cover and precipitation using the Special Sensor Microwave Imager. *Journal of Geophysical Research*, *96*(D4), 7423–7435.

Grody, N. C., & Weng, F. (2008). Microwave emission and scattering from deserts: Theory compared with satellite measurements. *IEEE Transactions on Geoscience and Remote Sensing*, *46*(2), 361–375.

Gu, X., & Tong, X. (2015). Overview of China Earth observation satellite programs [Space Agencies]. *IEEE Geoscience and Remote Sensing Magazine*, *3*(3), 113–129.

Hou, A. Y., Kakar, R. K., Neeck, S., Azarbarzin, A. A., Kummerow, C. D., Kojima, M., et al. (2014). The global precipitation measurement mission. *Bulletin of the American Meteorological Society*, *95*(5), 701–722.

Huffman, G. J., Bolvin, D. T., Braithwaite, D., Hsu, K., Joyce, R., Xie, P., & Yoo, S.-H. (2015). NASA Global Precipitation Measurement (GPM) Integrated Multi-satellite retrievals for GPM (IMERG). Algorithm Theoretical Basis Document, Version2, 4.

Huffman, G. J., Bolvin, D. T., Nelkin, E. J., Wolff, D. B., Adler, R. F., Gu, G., et al. (2007). The TRMM Multisatellite Precipitation Analysis (TMPA): Quasi-global, multiyear, combined-sensor precipitation estimates at fine scales. *Journal of Hydrometeorology*, *8*(1), 38–55.

Jackson, T. J. (1993). III. Measuring surface soil moisture using passive microwave remote sensing. *Hydrological Processes*, *7*(2), 139–152.

Joyce, R. J., Janowiak, J. E., Arkin, P. A., & Xie, P. (2004). CMORPH: A method that produces global precipitation estimates from passive microwave and infrared data at high spatial and temporal resolution. *Journal of Hydrometeorology*, *5*(3), 487–503.

Kawanishi, T., Sezai, T., Ito, Y., Imaoka, K., Takeshima, T., Ishido, Y., et al. (2003). The Advanced Microwave Scanning Radiometer for the Earth Observing System (AMSR-E), NASDA's contribution to the EOS for global energy and water cycle studies. *IEEE Transactions on Geoscience and Remote Sensing*, *41*(2), 184–194.

Kelley, O. A. (2014). Where the least rainfall occurs in the Sahara Desert, the TRMM radar reveals a different pattern of rainfall each season. *Journal of Climate*, *27*(18), 6919–6939.

Kubota, T., Shige, S., Hashizume, H., Aonashi, K., Takahashi, N., Seto, S., et al. (2007). Global precipitation map using satellite-borne microwave radiometers by the GSMaP Project: Production and validation. *IEEE Transactions on Geoscience and Remote Sensing*, *45*(7), 2259–2275.

Kummerow, C. D., Olson, W. S., & Giglio, L. (1996). A simplified scheme for obtaining precipitation and vertical hydrometeor profiles from passive microwave sensors. *IEEE Transactions on Geoscience and Remote Sensing*, *34*(5), 1213–1232.

Kummerow, C. D., Randel, D. L., Kulie, M., Wang, N.-Y., Ferraro, R., Joseph Munchak, S., & Petkovic, V. (2015). The evolution of the Goddard profiling algorithm to a fully parametric scheme. *Journal of Atmospheric and Oceanic Technology*, *32*(12), 2265–2280.

Kummerow, C. D., Ringerud, S., Crook, J., Randel, D., & Berg, W. (2011). An observationally generated a priori database for microwave rainfall retrievals. *Journal of Atmospheric and Oceanic Technology*, *28*(2), 113–130.

Laviola, S., & Levizzani, V. (2011). The 183-WSL fast rain rate retrieval algorithm: Part I: Retrieval design. *Atmospheric Research*, *99*(3), 443–461.

Levizzani, V., Kidd, C., Aonashi, K., Bennartz, R., Ferraro, R. R., Huffman, G. J., et al. (2018). The activities of the International Precipitation Working Group. *Quarterly Journal of the Royal Meteorological Society*, *144*, 3–15.

Li, R., & Min, Q. (2013). Dynamic response of microwave land surface properties to precipitation in Amazon rainforest. *Remote Sensing of Environment*, *133*, 183–192.

Liu, G. (2008). A database of microwave single-scattering properties for nonspherical ice particles. *Bulletin of the American Meteorological Society*, *89*(10), 1563–1570.

Liu, G., & Curry, J. A. (1992). Retrieval of precipitation from satellite microwave measurement using both emission and scattering. *Journal of Geophysical Research*, *97*(D9), 9959–9974.

Maggioni, V., Meyers, P. C., & Robinson, M. D. (2016). A review of merged high-resolution satellite precipitation product accuracy during the Tropical Rainfall Measuring Mission (TRMM) era. *Journal of Hydrometeorology*, *17*(4), 1101–1117.
Marchand, R., Mace, G. G., Ackerman, T., & Stephens, G. (2008). Hydrometeor detection using CloudSat—An Earth-orbiting 94-GHz cloud radar. *Journal of Atmospheric and Oceanic Technology*, *25*(4), 519–533.
Marshal, J. P., Krausman, P. R., Bleich, V. C., Ballard, W. B., & McKeever, J. S. (2002). Rainfall, El Nino, and dynamics of mule deer in the Sonoran Desert, California. *Journal of Wildlife Management*, *66*, 1283–1289.
Munchak, S. J., Ringerud, S., Brucker, L., You, Y., de Gelis, I., & Prigent, C. (2020). An active-passive microwave land surface database From GPM. *IEEE Transactions on Geoscience and Remote Sensing*. https://doi.org/10.1109/TGRS.2020.2975477
Nafus, M. G., Tuberville, T. D., Buhlmann, K. A., & Todd, B. D. (2017). Precipitation quantity and timing affect native plant production and growth of a key herbivore, the desert tortoise, in the Mojave Desert. *Climate Change Responses*, *4*(1), 4.
Norouzi, H., Rossow, W., Temimi, M., Prigent, C., Azarderakhsh, M., Boukabara, S., & Khanbilvardi, R. (2012). Using microwave brightness temperature diurnal cycle to improve emissivity retrievals over land. *Remote Sensing of Environment*, *123*, 470–482.
Petty, G. W. (1995). The status of satellite-based rainfall estimation over land. *Remote Sensing of Environment*, *51*(1), 125–137.
Prakash, S., Norouzi, H., Azarderakhsh, M., Blake, R., Prigent, C., & Khanbilvardi, R. (2018). Estimation of consistent global microwave land surface emissivity from AMSR-E and AMSR2 observations. *Journal of Applied Meteorology and Climatology*, *57*(4), 907–919.
Prigent, C., Aires, F., & Rossow, W. B. (2006). Land surface microwave emissivities over the globe for a decade. *Bulletin of the American Meteorological Society*, *87*(11), 1573–1584.
Sano, P., Casella, D., Mugnai, A., Schiavon, G., Smith, E. A., & Tripoli, G. J. (2013). Transitioning from CRD to CDRD in Bayesian retrieval of rainfall from satellite passive microwave measurements: Part 1. Algorithm description and testing. *IEEE Transactions on Geoscience and Remote Sensing*, *51*(7), 4119–4143.
Skofronick-Jackson, G., Petersen, W. A., Berg, W., Kidd, C., Stocker, E. F., Kirschbaum, D. B., et al. (2017). The global precipitation measurement (GPM) mission for science and society. *Bulletin of the American Meteorological Society*, *98*(8), 1679–1695.
Spencer, R. W., Goodman, H. M., & Hood, R. E. (1989). Precipitation retrieval over land and ocean with the SSM/I: Identification and characteristics of the scattering signal. *Journal of Atmospheric and Oceanic Technology*, *6*(2), 254–273.
Spencer, R. W., Martin, D. W., Hinton, B. B., & Weinman, J. A. (1983). Satellite microwave radiances correlated with radar rain rates over land. *Nature*, *304*(5922), 141.
Stephens, G. L., Vane, D. G., Boain, R. J., Mace, G. G., Sassen, K., Wang, Z., et al. (2002). The CloudSat mission and the A-Train: A new dimension of space-based observations of clouds and precipitation. *Bulletin of the American Meteorological Society*, *83*(12), 1771–1790. https://doi.org/10.1175/BAMS-83-12-1771
Turk, F. J., Haddad, Z. S., & You, Y. (2014). Principal components of multifrequency microwave land surface emissivities. Part I: Estimation under clear and precipitating conditions. *Journal of Hydrometeorology*, *15*(1), 3–19.
Vale, C. G., & Brito, J. C. (2015). Desert-adapted species are vulnerable to climate change: Insights from the warmest region on Earth. *Global Ecology and Conservation*, *4*, 369–379.
Wang, Y., You, Y., & Kulie, M. (2018). Global virga precipitation distribution derived from three spaceborne radars and its contribution to the false radiometer precipitation detection. *Geophysical Research Letters*, *45*, 4446–4455. https://doi.org/10.1029/2018GL077891
Wilheit, T. T. (1986). Some comments on passive microwave measurement of rain. *Bulletin of the American Meteorological Society*, *67*(10), 1226–1232.
Xie, P., Joyce, R., Wu, S., Yoo, S.-H., Yarosh, Y., Sun, F., & Lin, R. (2017). Reprocessed, bias-corrected CMORPH global high-resolution precipitation estimates from 1998. *Journal of Hydrometeorology*, *18*(6), 1617–1641.
Yin, J., Zhan, X., Liu, J., & Schull, M. (2019). An intercomparison of Noah model skills with benefits of assimilating SMOPS blended and individual soil moisture retrievals. *Water Resources Research*, *55*, 2572–2592. https://doi.org/10.1029/2018WR024326
You, Y., & Liu, G. (2012). The relationship between surface rainrate and water paths and its implications to satellite rainrate retrieval. *Journal of Geophysical Research*, *117*, D13207. https://doi.org/10.1029/2012JD017662
You, Y., Peters-Lidard, C., Wang, N.-Y., Turk, J., Ringerud, S., Yang, S., & Ferraro, R. (2018). The instantaneous retrieval of precipitation over land by temporal variation at 19 GHz. *Journal of Geophysical Research: Atmospheres*, *123*, 9279–9295. https://doi.org/10.1029/2017JD027596
You, Y., Petkovic, V., Tan, J., Kroodsma, R., Berg, W., Kidd, C., & Peters-Lidard, C. (2020). Evaluation of V05 precipitation estimates from GPM constellation radiometers using KuPR as the reference. *Journal of Hydrometeorology*, *21*(4), 705–728.
You, Y., Turk, F. J., Haddad, Z. S., Li, L., & Liu, G. (2014). Principal components of multifrequency microwave land surface emissivities. Part II: Effects of previous-time precipitation. *Journal of Hydrometeorology*, *15*(1), 20–37.
You, Y., Wang, N.-Y., & Ferraro, R. (2015). A prototype precipitation retrieval algorithm over land using passive microwave observations stratified by surface condition and precipitation vertical structure. *Journal of Geophysical Research: Atmospheres*, *120*, 5295–5315. https://doi.org/10.1002/2014JD022534
You, Y., Wang, N.-Y., Ferraro, R., & Meyers, P. (2016). A prototype precipitation retrieval algorithm over land for ATMS. *Journal of Hydrometeorology*, *17*(5), 1601–1621.
You, Y., Wang, N.-Y., Ferraro, R., & Rudlosky, S. (2017). Quantifying the snowfall detection performance of the GPM Microwave Imager channels over land. *Journal of Hydrometeorology*, *18*(3), 729–751.
You, Y., Wang, N.-Y., Kubota, T., Aonashi, K., Shige, S., Kachi, M., et al. (2020). Comparison of TRMM Microwave Imager rainfall datasets from NASA and JAXA. *Journal of Hydrometeorology*, *21*(3), 377–397.